Multiscale modeling of elasto-viscoplastic polycrystals subjected to finite deformations

Karel Matouš[†]

*Department of Aerospace and Mechanical Engineering, University of Notre Dame,
367 Fitzpatrick Hall of Engineering, Notre Dame, IN 46556-5637, USA*

Antoinette M. Maniatty

*Department of Mechanical, Aerospace, and Nuclear Engineering, Rensselaer Polytechnic Institute,
110 8th Street, Troy, NY 12180, UAS*

Abstract. In the present work, the elasto-viscoplastic behavior, interactions between grains, and the texture evolution in polycrystalline materials subjected to finite deformations are modeled using a multiscale analysis procedure within a finite element framework. Computational homogenization is used to relate the grain (meso) scale to the macroscale. Specifically, a polycrystal is modeled by a material representative volume element (RVE) consisting of an aggregate of grains, and a periodic distribution of such unit cells is considered to describe material behavior locally on the macroscale. The elastic behavior is defined by a hyperelastic potential, and the viscoplastic response is modeled by a simple power law complemented by a work hardening equation. The finite element framework is based on a Lagrangian formulation, where a kinematic split of the deformation gradient into volume preserving and volumetric parts together with a three-field form of the Hu-Washizu variational principle is adopted to create a stable finite element method. Examples involving simple deformations of an aluminum alloy are modeled to predict inhomogeneous fields on the grain scale, and the macroscopic effective stress-strain curve and texture evolution are compared to those obtained using both upper and lower bound models.

Keywords: multiscale modeling; finite deformations; elasto-viscoplastic; polycrystalline materials.

1 Introduction

Since the pioneering work of (Taylor and Elam 1925, Taylor 1938) and (Bishop and Hill 1951a, b), it has been widely recognized that phenomena occurring at the grain scale have a major impact on the macroscopic behavior of polycrystalline metals and that crystal plasticity models that capture these phenomena lead to more accurate predictions of the overall material response. As a result, numerous researchers have developed constitutive models for single crystals and have tried to relate these models to the overall behavior of polycrystalline metals. For example, (Peirce *et al.* 1983) and (Mathur and Dawson 1989) proposed models incorporating viscoplasticity and hardening effects.

---

† Associate Professor, Corresponding author, E-mail: kmatous@nd.edu

More recently, models that include grain size effects through gradient plasticity theories have been proposed, for example the models presented in (Acharya and Beaudoin 2000) and (Busso *et al.* 1999).

In order to predict the overall material response, in addition to modeling the individual grains, it is also necessary to model their interactions in a polycrystalline aggregate. A common approach is to assume the grains undergo homogeneous deformations based on some grain interaction assumption, such as the Taylor hypothesis (Taylor 1938) where each grain is assumed to undergo the same deformation (Mathur and Dawson 1989, Asaro and Needleman 1985, Maniatty *et al.* 1992), or another hypothesis, such as an equilibrium approach (Chastel and Dawson 1993) or a self-consistent approach (Molinari *et al.* 1987). While such models have provided some useful approximations of overall behavior, they are not capable of predicting the important effects due to the heterogeneous deformations that must occur on the grain scale in order to satisfy equilibrium and compatibility simultaneously and that have been well documented experimentally (Bay *et al.* 1992). For example, the gradients needed for capturing the grain size effects (Acharya and Beaudoin 2000, Busso *et al.* 1999) and the formation of subgrain nucleation sites for recrystallization are not predicted with such a model. In order to overcome these limitations, several researchers have implemented crystal plasticity models into finite element formulations to model discretized grain structures (Busso *et al.* 1999, Harren and Asaro 1989, Becker 1991, Bronkhorst *et al.* 1992, Marin and Dawson 1998, Sarma *et al.* 2002, Beaudoin *et al.* 2000). However, in those works, the boundary conditions were limited to homogeneous displacements and tractions, which do not represent the actual conditions on a polycrystalline aggregate at a material point that is adjacent to similar polycrystalline aggregates. Thus, only the results from grains away from the boundaries can be considered when evaluating the response in such cases. For example, in Clayton and McDowell (2003), a 2-D polycrystalline aggregate with a periodic structure is replicated in a 3 × 3 grid and only the center replica is used to evaluate the polycrystalline aggregate response. Such an approach requires the evaluation of nine times as many degrees of freedom as would seem necessary if appropriate boundary conditions could be applied. Therefore, in this work, a multiscale analysis approach is taken where the grain (meso) scale is characterized by a representative volume element (RVE), which contains a polycrystalline aggregate with a periodic structure. The pioneering contributions in the area of multiscale analysis for elastic inhomogeneous solids by Hashin and Shtrikman (1962) and Hill (1963) are well know. However, much less is understood for materials exhibiting a nonlinear response, such as the case for plasticity, although, rigorous bounds and estimates have been proposed by Willis (1989) for nonlinear behavior based on an energy potential and by Teply and Dvorak (1988) for incremental constitutive modeling. The general homogenization approach based on average theorems has been outlined by Hill (1984, 1985). These theories lead to a direct meso to macro transition, where deformations on the mesostructure are linked with the local deformation of the macro-continuum. Another group of models published in recent years devoted to multiscale modeling of heterogeneous systems at small and finite strains are the works of Michel *et al.* (1999), Miehe *et al.* (1998, 2002) and Kouznetsova *et al.* (2002). Recently, Kristensson *et al.* (2003) present a parallel finite element approach for analyzing micromechanical problems with periodic unit cells. In that work, a rate based finite element approach is used as a basis and an idealized, hexagonal periodic grain structure is analyzed. The work presented in (Sundararaghavana and Zabaras 2006, Ranganathan and Ostoja-Starzewski 2008) also deserves an attention.

In the present work, the elasto-viscoplastic behavior, interactions between grains, and the texture evolution in polycrystalline materials under finite strains are modeled using a multiscale analysis procedure within a finite element framework. We focus in this work on the physics behind the

equations, the efficient numerical implementation within the three-field variational method and on the proper kinematic decomposition due to both elastic and plastic incompatibilities. A realistic grain structure, motivated by experimental observations, is modeled by a unit cell consisting of a small number of grains. A periodic distribution of such RVEs is considered to describe material behavior locally on the macroscale. Section 2 describes mesoscale and macroscale kinematic relations based on Hill's averaging theorem and the resulting kinematic conditions on the RVE. In Section 3, some links between the mesoscale and macroscale behavior are derived and discussed based on the kinematic relations defined in Section 2, an energy condition, and the physical phenomena occurring at the mesoscale that drive the macroscale response. The computational approach and further details of the elastic and viscoplastic constitutive behavior are presented in Section 4. The elastic behavior is defined by a hyperelastic potential and the viscoplastic response is modeled by a simple power law complemented by a work hardening equation. The finite element framework is based on a Lagrangian formulation, where a kinematic split of the deformation gradient into volume preserving and volumetric parts together with a three-field form of the Hu-Washizu variational principle is adopted to create a stable finite element method. Finally, examples involving plane strain compression and simple shear of an aluminum alloy are modeled, and the macroscopic effective stress-strain curve and texture evolution are compared to those from Taylor and lower bound (equilibrium) models. The inhomogeneous, periodic meso-fields are presented, results are discussed, conclusions are drawn, and future work is outlined.

For clarification, the notation adopted in this paper denotes the tensor product between two second-order tensors, S and E for example, as SE and the scalar product as $S:E$. A quantity marked by an underline, $\underline{F}$, denotes the quantity F at the macroscale. Other notational conventions adopted in this paper are introduced as they are used.

2. Mesoscale-macroscale kinematic relationship

In this section, a theoretical framework is presented for relating the deformation at the mesoscale to that at the macroscale in order to describe the mechanical behavior of a homogenized macrostructure of characteristic length l_{macro} with a point-wise attached polycrystalline aggregate (meso-continuum) of characteristic length l_{meso} as shown in Fig. 1. It is assumed that $l_{meso} << l_{macro}$, and that a polycrystalline aggregate beyond a certain minimum size exhibits similar overall behavior despite mesoscale heterogeneities. Therefore, the macro-level is identified by a certain representative sample (RVE), which can be treated mathematically at the macro-level as a homogeneous system. In this work, computational homogenization is used to link the mesoscale to the macroscale.

First, let $\underline{\phi}(X, t)$ denotes the motion of the macro-continuum at the current time $t \in \mathbb{R}^+$, and let $\underline{F}(X, t) = \underline{\nabla}\,\underline{\phi}(X, t)$ be the deformation gradient with the Jacobian given by $\underline{J} = \det(\underline{F})$. Here, $\underline{X} \in \mathbb{R}^3$ designates the position of a macroscale particle in the reference configuration $\underline{B}_0 \subset \mathbb{R}^3$ with respect to a Cartesian coordinate system. Next, consider the motion $\phi(X, t)$ of the mesocontinuum, and let $F(X, t) = \nabla\,\phi(X, t)$ represent the meso-deformation gradient with the Jacobian given by $J = \det(F)$. Here $X \in \mathbb{R}^3$ designates the position of a mesoscale particle in the reference configuration $B_0 \subset \mathbb{R}^3$ with respect to a Cartesian coordinate system. Moreover, the mesoscale deformation is assumed to be driven by the macro-deformation $\underline{F}$ such that the spatial coordinates of a particle at the mesoscale are given by
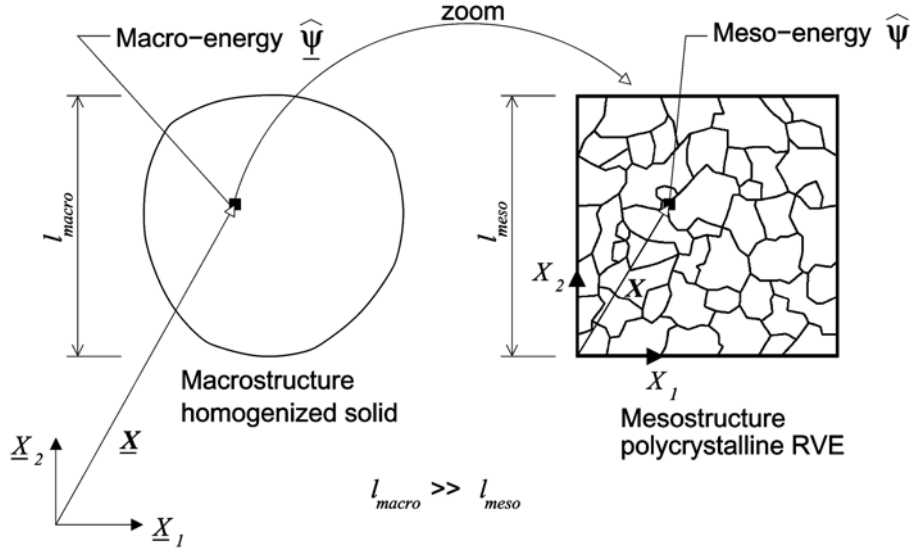
Fig. 1 Homogenized macro-continuum and periodic polycrystalline mesostructure
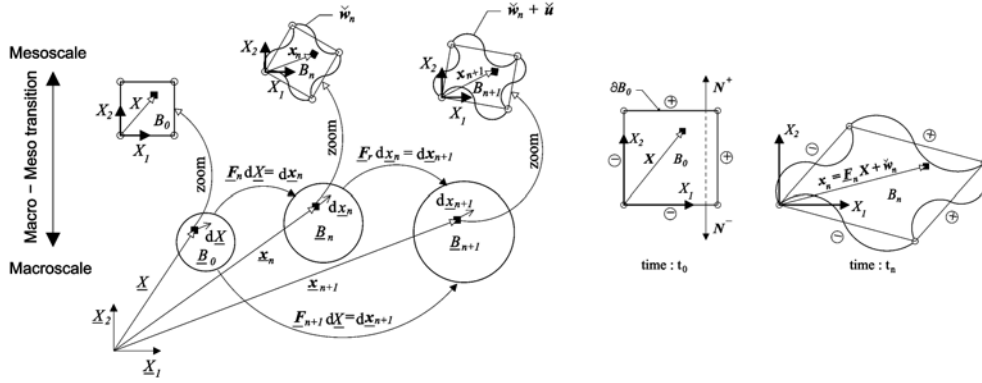

Fig. 2 a) Macro-to-Meso transition   Fig. 2 b) Periodic fluctuation field

$$x = \underline{F}X + \breve{w} \tag{1}$$

where $\breve{w}$ denotes the fluctuation in the displacement field on the mesoscale as displayed in Fig. 2a. Note that because $l_{meso} << l_{macro}$, an infinitesimal fiber $d\underline{X}$ on the macroscale is treated as just X on the mesoscale where X is a position vector lying within the RVE. The deformation gradient on the mesoscale is then

$$F = \underline{F} + \nabla \breve{w} \tag{2}$$

where ∇ operating on a mesoscale quantity is the gradient operator with respect to X.

The macroscopic and mesoscopic deformation gradients are related via a volume average (Hill 1984, 1985)

$$\underline{F} = \frac{1}{V_0} \int_{B_0} F dV_0 \tag{3}$$

After applying Gauss' theorem and assuming a mesostructure without cavities, one obtains

$$\underline{F} = \frac{1}{V_0} \int_{\partial B_0} x \otimes N \mathrm{d}A_0 \tag{4}$$

where N is the outward normal of the meso-system at $X \in \partial B_0$ with ∂B_0 being the boundary of B_0.

In addition, introducing Eqs. (1) and (2) into (3) and (4), the following constraint on the fluctuation field results

$$\frac{1}{V_0} \int_{\partial B_0} \breve{w} \otimes N \mathrm{d}A_0 = 0 \; \Rightarrow \; \frac{1}{V_0} \int_{B_0} \nabla \breve{w} \mathrm{d}V_0 = 0 \tag{5}$$

A key assumption in homogenization theory is that the statistical sample (RVE) is representative of some neighborhood of material points and thus can be treated as locally periodic. Assuming a periodic fluctuation in the displacement field over the RVE results in the following non-trivial periodic boundary conditions

$$\breve{w}(X^+) = \breve{w}(X^-) \text{ on } \partial B_0 \tag{6}$$

where the boundary ∂B_0 is decomposed as $\partial B_0 = \partial B_0^+ \cup \partial B_0^-$ with normals $N^+ = -N^-$ at two associated points $X^+ \in \partial B_0^+$ and $X^- \in \partial B_0^-$. Furthermore, since the corners of the RVE $X_\beta^c \in \partial B_0$, $\beta = 1, 4$ must all have the same displacement fluctuation $\breve{w}(X_\beta^c)$ due to the double periodicity (see Fig. 2b), a non-zero value would just correspond to a rigid translation. Thus

$$\breve{w}(X_\beta^c) = 0, \qquad x_\beta^c = \underline{F} X_\beta^c, \qquad \beta = 1, 4 \tag{7}$$

at the corners. Therefore, the positions of the corners of the RVE are completely prescribed by their positions in the reference configuration and the macroscopic deformation gradient. The periodic displacement fluctuation is illustrated in Fig. 2b.

The above kinematic description together with a set of governing equations, including equilibrium and elasto-viscoplastic constitutive equations, defines a boundary value problem on the mesoscale. Assuming a prescribed macroscopic deformation gradient, the boundary value problem can be solved using the finite element method as described in Section 4. However, it is also of interest to relate the mesoscale response to the macroscopic behavior, which is described next.

3. Links between the mesoscale and macroscale behavior

The behavior at the macroscale can be linked to the mesoscale through the following energy condition. The potential energy on the meso- and macroscales are minimized when the following condition of stationarity is met

$$\inf_{\underline{F}} \hat{\underline{\psi}}(\underline{F}) = \inf_{\underline{F}} \inf_{\breve{w}} \frac{1}{V_0} \int_{B_0} \hat{\underline{\psi}}(\underline{F} + \nabla \breve{w}) \mathrm{d}V_0 \tag{8}$$

and

$$\underline{F} \in L^+$$

$$\breve{w} \in U := \{U \subset [W^{1,s}]^{\Re}\}, \breve{w} \text{ periodic on } \partial B_0$$

where $\hat{\psi}$ and $\hat{\underline{\psi}}$ represent the free energy density on the meso- and macroscales, respectively, L^+ is the space of second order tensors with positive determinant, $W^{1,s}$ denotes a certain Sobolev space, and $\mathfrak{N}$ is the space dimension. Note that we make no attempt to address issues of existence and uniqueness of the solution. We proceed under the assumptions that the boundary value problem in question admits a solution in some sense in spaces defined above, and given this, we continue to construct the numerical approximation of the solution, and replace the continuous spaces by their discrete counterparts.

In addition, the elastic constitutive laws relating the first Piola-Kirchhoff stress to the free energy on the mesoscale and macroscale are

$$\boldsymbol{P} = \frac{\partial \hat{\psi}}{\partial \boldsymbol{F}} \text{ and } \underline{\boldsymbol{P}} = \frac{\partial \hat{\underline{\psi}}}{\partial \underline{\boldsymbol{F}}} \tag{9}$$

respectively. Applying standard variational principles to Eq. (8), using (2) and (9), and keeping in mind that variations of the macroscale deformation gradient $\delta \underline{\boldsymbol{F}}$ and the mesoscale fluctuation displacements $\delta \check{\boldsymbol{w}}$ are independent, we arrive at the usual variational energy condition (see, for example, the following references (Hill 1985, Miehe *et al.* 1998, Kouznetsova *et al.* 2002))

$$\mathcal{R}_{\underline{F}} = \left[\frac{1}{V_0} \int_{B_0} \boldsymbol{P} \mathrm{d}V_0 - \underline{\boldsymbol{P}} \right] : \delta \underline{\boldsymbol{F}} = 0$$

$$\mathcal{R}_{\check{w}} = \frac{1}{V_0} \int_{B_0} \boldsymbol{P} : \nabla \delta \check{\boldsymbol{w}} \mathrm{d}V_0 = 0 \tag{10}$$

with

$$\delta \underline{\boldsymbol{F}} \in L$$

$$\delta \check{\boldsymbol{w}} \in U, \ \delta \check{\boldsymbol{w}} = 0 \text{ on } \partial B_0$$

where L is the space of second order tensors. In other words, the volume average of the variation of the work performed on the RVE equals the local variation of the work on the macroscale, and the mesoscale fluctuation field does not contribute to the average variation in the work. Furthermore, due to the arbitrariness of $\delta \underline{\boldsymbol{F}}$, Eq. (10a) indicates that the macroscopic first Piola-Kirchhoff stress equals the volume average of the first Piola-Kirchhoff stress at the mesoscale. It should also be noted that Eq. (10b) is the weak form of the equilibrium equation on the mesoscale for purely kinematic boundary conditions (as is the case here). Note that we do not assume the body forces in (8) and (10), respectively.

In addition, due to the periodicity assumption and in order to satisfy equilibrium with the assumed neighboring RVEs, the tractions on the boundary of the RVE, ∂B_0, will also be periodic. Thus, the tractions $\check{\boldsymbol{t}}(\boldsymbol{X}) = \boldsymbol{P}(\boldsymbol{X})\boldsymbol{N}(\boldsymbol{X})$ will satisfy

$$\check{\boldsymbol{t}}(\boldsymbol{X}^+) = -\check{\boldsymbol{t}}(\boldsymbol{X}^-) \text{ on } \partial B_0 \tag{11}$$

Now, it remains to define the viscoplastic part of the constitutive equations on the mesoscale, which, together with the elastic constitutive law on this scale, dictates the relationship between the stress and deformation on the mesoscale directly, and, through averaging, on the macroscale too. First, a multiplicative split of the deformation gradient into elastic (lattice) and plastic parts is assumed at the mesoscale (Lee 1969, Hill 1966) with the plastic part being isochoric giving (Fig. 3)
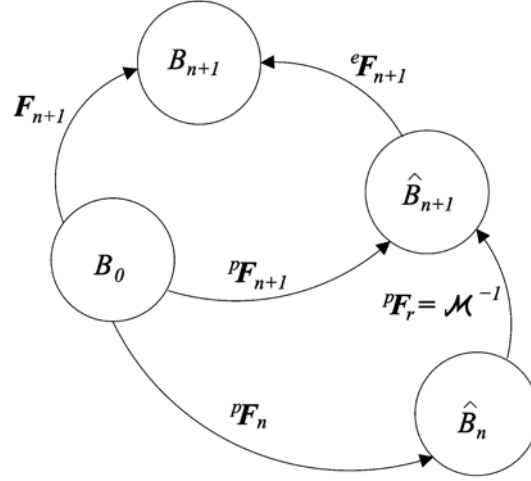
Fig. 3 Kinematic decomposition of mesoscale deformation gradients

$$\boldsymbol{F} = {}^{e}\boldsymbol{F}\,{}^{p}\boldsymbol{F} \quad \det({}^{p}\boldsymbol{F}) = 1 \tag{12}$$

where left superscripts e and p indicate the elastic and plastic parts, respectively. The viscoplastic part of the deformation is assumed to be due to slip along crystallographic slip systems. The constitutive behavior for the crystallographic slip is governed by a general flow equation together with an evolution equation for the resistance to flow (i.e. hardening). The form of these relationships is as follows

$$^{p}\hat{\boldsymbol{L}} \equiv {}^{p}\dot{\boldsymbol{F}}\,{}^{p}\boldsymbol{F}^{-} = \sum_{\alpha=1}^{\mathcal{N}_{s}} \dot{\gamma}^{\alpha}\mathcal{P}^{\alpha} \tag{13}$$

$$\dot{\gamma}^{\alpha} = \dot{\gamma}(\tau^{\alpha}, g) \tag{14}$$

$$\dot{g} = G(\dot{\gamma}, g)\dot{\gamma}, \dot{\gamma} = \sum_{\alpha=1}^{\mathcal{N}_{s}} |\dot{\gamma}^{\alpha}| \tag{15}$$

where

$$\tau^{\alpha} = ({}^{e}\boldsymbol{F}^{T}\,\boldsymbol{P}\,{}^{p}\boldsymbol{F}^{T}){:}\mathcal{P}^{\alpha} \tag{16}$$

In Eqs. (13-16) $^{p}\hat{\boldsymbol{L}}$ is the plastic velocity gradient on the intermediate configuration $\hat{\boldsymbol{B}}$ (Fig. 3), $\mathcal{N}_{s}$ is the number of slip systems, g is the resistance to flow on the slip systems, G is the hardening function, $\dot{\gamma}^{\alpha}$ is the rate of shear, τ^{α} is the resolved shear stress, and $\mathcal{P}^{\alpha}$ is the Schmid tensor, where superscript α indicates the slip system. It should be noted that in this work, the latent and self hardening are assumed to be equal giving the same resistance to plastic flow, g, on all the slip systems. Further details of the mesoscale viscoplastic constitutive law considered herein are given in Section 4.

An incrementally linearized form of the macroscopic constitutive equation can be defined by linearizing the nonlinear Eqs. (10) where the mesoscale constitutive laws are used to relate the deformation gradient on the mesoscale, $\boldsymbol{F} + \nabla \check{\boldsymbol{w}}$, to the first Piola-Kirchhoff stress on the mesoscale $\boldsymbol{P}$. Linearization of Eqs. (10) yields

$$\begin{bmatrix} \mathcal{K}_{11} & \mathcal{K}_{12} \\ \mathcal{K}_{21} & \mathcal{K}_{22} \end{bmatrix}^k \begin{Bmatrix} \Delta\underline{F} \\ \Delta\breve{w} \end{Bmatrix} = \begin{Bmatrix} \underline{P} \\ 0 \end{Bmatrix}^{k+1} - \begin{Bmatrix} \underline{P} \\ \mathcal{R}_2 \end{Bmatrix}^k \tag{17}$$

where

$$\delta\underline{F}{:}\mathcal{K}_{11} \equiv \frac{\partial\mathcal{R}_F}{\partial\underline{F}}, \; \delta\underline{F}{:}\mathcal{K}_{12} \equiv \frac{\partial\mathcal{R}_F}{\partial\breve{w}}, \; \delta\breve{w}{:}\mathcal{K}_{21} \equiv \frac{\partial\mathcal{R}_w}{\partial\underline{F}}, \; \delta\breve{w}{:}\mathcal{K}_{22} \equiv \frac{\partial\mathcal{R}_{\breve{w}}}{\partial\breve{w}}, \; \delta\breve{w}\cdot\mathcal{R}_2 \equiv \mathcal{R}_{\breve{w}}$$

and for the $(k+1)$-th iteration, the macroscopic deformation gradient, the meso-continuum fluctuation displacement field, and the macroscopic first Piola-Kirchoff stress are updated as $\underline{F}^{k+1} = \underline{F}^k + \Delta\underline{F}$, $\breve{w}^{k+1} = \breve{w}^k + \Delta\breve{w}$, and $\underline{P}^{k+1} = \underline{P}^k + \Delta\underline{P}$, respectively. Eliminating the periodic displacements $\Delta\breve{w}$ from Eq. (17) provides the incrementally linear macroscopic constitutive law

$$\Delta\underline{P} = \underline{\mathfrak{L}}{:}\Delta\underline{F} - (\mathcal{K}_{12}\mathcal{K}_{22}^{-1})^k{:}\mathcal{R}_2^k \tag{18}$$

where the tangent elasto-viscoplastic pseudo-moduli is

$$\underline{\mathfrak{L}} = (\mathcal{K}_{11} - \mathcal{K}_{12}\mathcal{K}_{22}^{-1}\mathcal{K}_{21})^k \tag{19}$$

Note that for a motion driven multiscale nested scheme, used in our case, $\Delta\underline{F}$ is applied and $\Delta\underline{P}$ is computed from (18) with $\mathcal{R}_2^k = 0$, since we numerically equilibrate (10)(b) at the mesoscale.

While the above linearized form for the macroscopic response is useful for computational purposes and may provide some insight, it is also of interest to see what other implications the kinematic and energy conditions, Eqs. (1-12), have on the macroscopic constitutive relations. First, consider the elastic-plastic kinematic relations. If we assume a multiplicative decomposition of the deformation gradient at the macroscale into a locally recoverable elastic deformation, ${}^e\underline{F}$, and a non-recoverable, inelastic deformation, ${}^*\underline{F}$, then combining with Eqs. (2) and (12) yields

$$\underline{F} = {}^e\underline{F}\,{}^*\underline{F} \text{ and } {}^e\mathbb{F}\,{}^p\mathbb{F} = {}^e\underline{F}\,{}^*\underline{F} + \nabla\breve{w} \tag{20}$$

Now, if the RVE is unloaded, i.e., $\breve{t} = \underline{P}\underline{N} = 0$ on $\partial\mathbb{B}$ where $\mathbb{B}$ refers to the unloaded mesoscale configuration, and recalling Eq. (10a), then the stresses on the RVE must be self-equilibrating residual stresses such that

$$\underline{P} = \frac{1}{V_0}\int_{B_0} \underline{P}\,dV_0 = 0 \tag{21}$$

This macroscopic, stress-free, intermediate configuration, $\hat{\underline{\mathcal{B}}}$, is reached upon hypothetical instantaneous elastic unloading from the current configuration $\underline{B}$ via the inverse of the macroscopic elastic deformation gradient, ${}^e\underline{F}^{-1}$ as shown in Fig. 4. Thus, the macroscopic inelastic deformation gradient is given by

$$^*\underline{F} = {}^e\underline{F}^{-1}\underline{F} = \frac{1}{V_0}\int_{B_0} {}^e\mathbb{F}\,{}^p\mathbb{F}\,dV_0 \tag{22}$$

where ${}^e\mathbb{F}$ and ${}^p\mathbb{F}$ represent the elastic and plastic residual deformation gradient fields on the hypothetically unloaded RVE.

Therefore ${}^*\underline{F}$ contains a combination of elastic and plastic residual deformations at the mesoscale, which are related to lattice incompatibilities. Specifically, let the position of particles on this unloaded RVE be denoted $\mathbb{X} \in \mathbb{B}$ and on the associated intermediate configuration $\hat{\mathbb{X}} \in \hat{\mathbb{B}}$. As
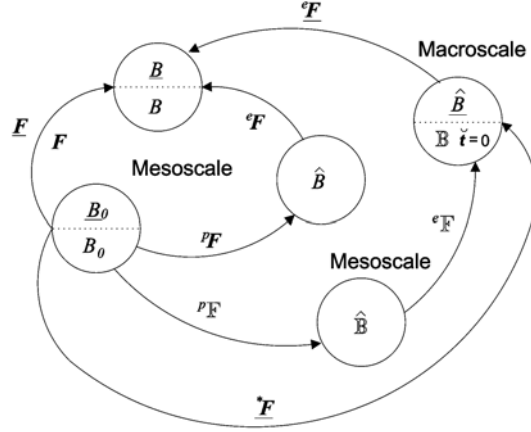
Fig. 4 Kinematic decomposition of deformation gradients at multiple length scales

pointed out by Lee (1981), due to heterogeneities on this scale, the mappings $\boldsymbol{X} \rightarrow \hat{\mathbb{X}}$ and $\hat{\mathbb{X}} \rightarrow \mathbb{X}$ are not continuous even though the mapping $\boldsymbol{X} \rightarrow \mathbb{X}$ is continuous. Thus, a closed loop on the undeformed configuration, B_0, would map to a closed loop on the deformed unloaded configuration, $\mathbb{B}$, but not to a closed loop on the intermediate configuration, $\hat{\mathbb{B}}$. Busso *et al.* (1999) and Acharya and Beaudoin (2000) both interpret this incompatibility within a grain as a net Burgers vector, $\boldsymbol{b}_c$, i.e.

$$\boldsymbol{b}_c = \oint_{C_0} {}^P\mathbb{F}\,\mathrm{d}\boldsymbol{X} = \oint_C {}^e\mathbb{F}^{-1}\,\mathrm{d}\mathbb{X} \tag{23}$$

where curve C_0 lies entirely within a single grain in B_0 and is mapped to $C \subset \mathbb{B}$. It should be noted that in Busso *et al.* (1999) and Acharya and Beaudoin (2000) the above calculation is done on the loaded RVE. If the hypothetical unloading is purely elastic on the RVE, then ${}^P\mathbb{F} = {}^P\boldsymbol{F}$, and there is no difference in the result whether Eq. (23) is computed on the loaded or unloaded RVE.

Because of the heterogeneities and resulting incompatibilities at the mesoscale, the relationship between the meso- and macroscale elastic and plastic deformation gradients (${}^e\boldsymbol{F}$ and ${}^P\boldsymbol{F}$) and (${}^e\underline{\boldsymbol{F}}$ and ${}^P\underline{\boldsymbol{F}}$) is not clear due to the elastic-plastic coupling at the smaller scale. Since the macroscopic non-recoverable deformation gradient ${}^*\underline{\boldsymbol{F}}$ contains both elastic (due to incompatibilities) and plastic residual deformations on the mesoscale, let

$$ {}^*\underline{\boldsymbol{F}} = {}^i\underline{\boldsymbol{F}}\,{}^P\underline{\boldsymbol{F}} \tag{24}$$

where ${}^i\underline{\boldsymbol{F}}$ is the macroscale part of the deformation gradient due to incompatibilities on the mesoscale. The unloaded RVE, $\mathbb{B}$, is arbitrary by a rigid rotation. Therefore, we can choose the macroscopic elastic deformation gradient to be symmetric, i.e., let

$$ {}^e\underline{\boldsymbol{F}} = {}^e\underline{\boldsymbol{F}}^T = {}^e\underline{\boldsymbol{V}} \tag{25}$$

Furthermore, performing a left polar decomposition on the lattice deformation gradient on the mesoscale gives

$$ \boldsymbol{F} = {}^e\boldsymbol{F}\,{}^P\boldsymbol{F} = {}^e\boldsymbol{V}\,{}^l\boldsymbol{R}\,{}^P\boldsymbol{F}, \qquad {}^e\boldsymbol{V} = {}^e\boldsymbol{V}^T \tag{26}$$

where ${}^l\boldsymbol{R}$ is the lattice rotation. Now, let the macroscopic plastic deformation gradient be the volume average of the mesoscale plastic deformation gradient with its first index pushed forward by the

lattice rotation so as to eliminate the effect of the varying intermediate configuration at the mesoscale, i.e.

$$^{p}\underline{F} = \frac{1}{V_0} \int_{B_0} {}^{l}R \, {}^{p}F \, dV_0 \tag{27}$$

Then the part of the deformation gradient at the macroscale due to the incompatibilities at the mesoscale, using Eqs. (22) and (24), is

$$^{i}\underline{F} = {}^{e}\underline{F}^{-1} \underline{F} \, {}^{p}\underline{F}^{-1} \tag{28}$$

where $^{e}\underline{F}$ can be determined by unloading the RVE, and $^{p}\underline{F}$ can be evaluated from Eq. (27).

Finally, it is interesting to note that just as the hypothetically unloaded RVE has a combination of elastic and plastic residual deformations due to heterogeneities on this scale making $\hat{\mathbb{B}}$ physically unattainable, likewise at the macroscale, the unloaded intermediate configuration $\hat{B}$ is typically not attainable due to heterogeneities on the larger scale, as discussed by Lee (1981).

4. Mesoscale model of polycrystal

In this section, the computational approach for modeling a polycrystalline aggregate (meso-continuum), based on the theory presented in Sections 2 and 3, is outlined. Further details of this formulation can be found in our earlier work (Matou and Maniatty 2004). Specifics of the elasto-viscoplastic constitutive behavior are also given in this section.

A kinematic split of the meso-deformation gradient into volume preserving and volumetric parts is used to create a stable finite element method in the context of nearly incompressible behavior (Simo *et al.* 1985, Hughes 1980). The volume preserving part of a meso-deformation gradient, denoted with an over-bar (−) is

$$\overline{F} = J^{-\frac{1}{3}} F = J^{-\frac{1}{3}} [\underline{F} + \nabla \check{w}] \tag{29}$$

and the volumetric part reads

$$\theta = J \tag{30}$$

Assuming an incremental formulation at the mesoscale and adopting the multiplicative decomposition of the deformation gradient into elastic and plastic parts (Lee 1969, Hill 1966), we arrive at (Fig. 3)

$$F_{n+1} = \theta_{n+1}^{\frac{1}{3}} \overline{F}_{n+1}$$

$$F_{n+1} = {}^{e}F_{n+1} \, {}^{p}F_{n+1} = \theta_{n+1}^{\frac{1}{3}} \, {}^{e}\overline{F}_{n+1} \, {}^{p}\overline{F}_{n+1}$$

$$^{e}F_{n+1} = F_{n+1} \, {}^{p}F_{n+1}^{-1} = \theta^{\frac{1}{3}} \, {}^{e}\overline{F}_{n+1} \, {}^{p}F_{n+1}^{-1}$$

$$^{p}F_{n+1} = {}^{p}F_r \, {}^{p}F_n = \mathcal{M}^{-1} \, {}^{p}F_n \tag{31}$$

where subscripts n and $n+1$ indicate quantities at times t_n and t_{n+1}, and subscript r indicates a relative quantity between times t_n and t_{n+1}.

Symbol θ is now an additional variable entering the formulation and denotes a mixed

representation for the determinant of the deformation gradient, $\theta \equiv \det(F)$. In the finite element formulation, Eq. (30) is satisfied in a weak sense to provide stability. Then the meso-deformation gradient is

set as $F_{n+1} = \theta_{n+1}^{\frac{1}{3}} \tilde{J}_{n+1}^{\frac{1}{3}} \tilde{F}_{n+1}$, $\tilde{J}_{n+1} = \det(\tilde{F}_{n+1})$, where over-tilde (~) denotes quantities calculated from finite element approximations of the displacement field, and θ_{n+1} is solved for explicitly in the mixed formulation.

In general, the Helmholtz free energy per unit volume stored in the system depends on the elastic behavior, plastic state of deformation, and temperature. For the sake of simplicity, we neglect thermal effects and adopt the usual assumption that the elastic potential is unaffected by the plastic flow. In addition, it is assumed that the elastic behavior is linear and elastic strains are small, typical for metals. Based on such observation, one can define the hyperelastic potential, referred to in Eqs. (8) and (9), as

$$\hat{\psi}(^{e}F) = \frac{1}{2} {}^{e}\hat{E} : \mathcal{L} : {}^{e}\hat{E} \tag{32}$$

and the mesoscale elastic constitutive stress strain relation on the relaxed configuration $\hat{B}$ reads

$$\hat{S} = 2\frac{\partial \hat{\psi}}{\partial {}^{e}\hat{C}} = \mathcal{L} : {}^{e}\hat{E} \tag{33}$$

where ${}^{e}\hat{C} = {}^{e}F^{T}\, {}^{e}F$ denotes the mesoscopic right Cauchy-Green tensor, ${}^{e}\hat{E} = \frac{1}{2}({}^{e}\hat{C} - 1)$ denotes the mesoscopic elastic Green-Lagrange tensor, $\mathcal{L}$ represents the fourth-order elasticity tensor at the meso-level, and $\mathbf{1}$ is the second-order identity tensor. The second Piola-Kirchoff (P-K) stress on $\hat{B}$, $\hat{S}$, can be expressed as the pull back of the Cauchy stress σ given by $\hat{S} = \det({}^{e}F)\, {}^{e}F^{-1}\, \sigma\, {}^{e}F^{-T}$ and can be related to the first Piola-Kirchhoff stress in Eq. (9), as $P = {}^{e}F\, \hat{S}\, {}^{p}F^{-T}$, which is defined on B_0. Using this relationship in Eq. (16), it is possible to express the resolved shear stress on slip system α as

$$\tau^{\alpha} = ({}^{e}\hat{C}\hat{S}) : \mathcal{P}^{\alpha} \tag{34}$$

We assume that crystallographic slip is the only mechanism for the plastic deformation. Such slip occurs due to dislocation motion through the crystal lattice. The form of the governing equations for the plastic part of the deformation is given in Eqs. (13-16). The specific form of the flow law used here is a simple power law, i.e.

$$\dot{\gamma}^{\alpha} = \dot{\gamma}_0 \frac{\tau^{\alpha}}{g} \left| \frac{\tau^{\alpha}}{g} \right|^{\frac{1}{m}-1} \tag{35}$$

where m is a material rate sensitivity parameter and $\dot{\gamma}_0$ is a reference rate. To describe the evolution of resistance to plastic slip, we adopt an approach proposed by Voce (1948) and later modified by Kocks (1976) and used in Mathur and Dawson (1989) and Maniatty *et al.* (1992) as follows

$$\dot{g} = G(\dot{\gamma}, g)\dot{\gamma} = G_0 \left(\frac{g_s - g}{g_s - g_0} \right) \dot{\gamma} \tag{36}$$

where a hardening rate G_0 and an initial resolved shear strength g_0 are material parameters. The saturation value of the hardness g_s is given by

$$g_s = g_{s_0} \left| \frac{\dot{\gamma}}{\dot{\gamma}_s} \right|^{\omega} \tag{37}$$

where g_{s_0}, $\dot{\gamma}_s$ and ω are material parameters.

For a prescribe deformation path, the stress response and hardness evolution can be obtained by integrating the constitutive equations presented above. The numerical procedure used in our computations employs a fully implicit two-level backward Euler integration scheme together with a modified Lagrange variational principle to enforce the plastic incompressibility. The detail description of the integration algorithm is given in our earlier work (Matou and Maniatty 2004).

As mentioned earlier, an incremental finite element formulation based on a kinematic split of the deformation gradient into volume-preserving and volumetric parts is used, Eqs. (31). The formulation uses a three-field form of the Hu-Washizu variational principle (Simo *et al.* 1985, Hughes 1980, Moran *et al.* 1990) to treat volume constraints arising from the nearly incompressible behavior due to the isochoric plastic flow, which dominates at large deformations. Here it is important to mention that the meso-deformation is driven by the macro-deformation as described in Sections 2 and 3. However, the dual formulation (stress-based approach) could also be used by solving the system given in Eq. (17).

First, let us recall that the spatial coordinates of a particle at the mesoscale are given by Eq. (1), which can be written incrementally as

$$x_{n+1} = \underline{F}_{n+1} X + \check{w}_n + \check{u}$$

where $\check{u} = \check{w}_{n+1} - \check{w}_n$ is the increment in the fluctuation field over the time step. The meso-continuum deformation gradient reads, Eq. (2)

$$F_{n+1} = \underline{F}_{n+1} + \nabla \check{w}_{n+1}$$

Next, referring to Eq. (8), consider the Lagrangian functional written as

$$\Pi_L(\check{u}, \theta, p) = \frac{1}{V_0} \frac{1}{2} \int_{B_0} {}^e\hat{E} : \mathcal{L} : {}^e\hat{E} \, dV_0 + \frac{1}{V_0} \int_{B_0} p(\tilde{J} - \theta) \, dV_0 \tag{38}$$

with

$$^e\hat{E} = \frac{1}{2} \left(\theta^{\frac{2}{3}} \tilde{J}^{-\frac{2}{3}p} F^T \tilde{F}^T \tilde{F} \,^p F^{-1} - 1 \right) \tag{39}$$

where p is a hydrostatic pressure. The condition of stationarity for the functional $\Pi_L(\check{u}, \theta, p)$ is given by

$$\begin{array}{ccc} \inf & \inf & \sup \quad \Pi_L(\check{u}, \theta, p) \\ \check{u} \in U & \theta \in Q & p \in Q \end{array} \tag{40}$$

and

$$\check{u} \text{ periodic on } \phi(\partial B_{\check{u}})$$

$$Q \subset L_2 \tag{41}$$

where $\phi(\partial B_{\check{u}})$ is the boundary on which the periodic displacements are prescribed. Following standard variational methods, the resulting system of non-linear equations on the mesoscale yields

$$\mathcal{R}_{\breve{u}} \equiv \frac{\partial \Pi_L}{\partial \breve{u}} \cdot \delta \breve{u} \ = \ \frac{1}{V_0} \int_{B_0} \left[\theta^{\frac{2}{3}} \tilde{J}^{-\frac{2}{3}} \boldsymbol{\mathcal{A}}(\delta \breve{u}) : \hat{\boldsymbol{S}} + p \tilde{J} \mathrm{tr}(\tilde{\boldsymbol{F}}^{-1} \nabla \delta \breve{u}) \right] \mathrm{d}V_0$$

$$\mathcal{R}_p \equiv \frac{\partial \Pi_L}{\partial p} \delta p \ = \ \frac{1}{V_0} \int_{B_0} (\tilde{J} - \theta) \delta p \, \mathrm{d}V_0$$

$$\mathcal{R}_\theta \equiv \frac{\partial \Pi_L}{\partial \theta} \delta \theta \ = \ \frac{1}{V_0} \int_{B_0} \left[\frac{1}{3} \theta^{-\frac{1}{3}} \tilde{J}^{-\frac{2}{3}} ({}^P\boldsymbol{F}^{-T} \tilde{\boldsymbol{F}}^T \tilde{\boldsymbol{F}} \, {}^P\boldsymbol{F}^{-1}) : \hat{\boldsymbol{S}} - p \right] \delta \theta \, \mathrm{d}V_0 \tag{42}$$

where $\delta \breve{u}$, δp, and $\delta \theta$ are arbitrary functions satisfying

$$\delta \breve{u} \in U, \qquad \delta \breve{u} = \boldsymbol{0} \text{ on } \phi(\partial B_{\breve{u}})$$

$$\delta p, \, \delta \theta \in Q \tag{43}$$

and

$$\boldsymbol{\mathcal{A}}(\delta \breve{u}) \ = \ {}^P\boldsymbol{F}^{-T} \left[(\nabla \delta \breve{u}^T \tilde{\boldsymbol{F}})^{\mathrm{sym}} - \frac{1}{3} \boldsymbol{F}^T \tilde{\boldsymbol{F}} \mathrm{tr}(\tilde{\boldsymbol{F}}^{-1} \nabla \delta \breve{u}) \right] {}^P\boldsymbol{F}^{-1} \tag{44}$$

A finite element solution of a system of non-linear equations, Eq. (42), involving a projection onto a finite-dimensional subspace requires a consistent linearization about a configuration $(\breve{u}, \theta, p)$, which can be represented symbolically as

$$D\mathcal{R}_{\breve{u}}[\Delta \breve{u}] + D\mathcal{R}_{\breve{u}}[\Delta p] + D\mathcal{R}_{\breve{u}}[\Delta \theta] = -\mathcal{R}_{\breve{u}}$$

$$D\mathcal{R}p[\Delta \breve{u}] + 0 - D\mathcal{R}p[\Delta \theta] = -\mathcal{R}p$$

$$D\mathcal{R}_\theta[\Delta \breve{u}] - D\mathcal{R}_\theta[\Delta p] + D\mathcal{R}_\theta[\Delta \theta] = -\mathcal{R}_\theta \tag{45}$$

The notation $\mathcal{R}_y^{k+1} \approx \mathcal{R}_y^k + D\mathcal{R}_y[\Delta y] = \boldsymbol{0}$ is employed for consistent linearization of a nonlinear equation $\mathcal{R}_y = \boldsymbol{0}$, where a solution $y^{k+1} = y^k + \Delta y$ at iteration $k+1$ is obtained using Newtons type iterative method. The system of linear equations, Eq. (45), is solved using sparse direct solver UMFPACK (Davis and Duff 1997, 1999). The detail description of the linearization procedure is presented in the paper by Matous and Maniatty (2004).

Finally, it should be noted that the periodicity conditions are considered as constraints imposed to the discrete unknowns in the finite element solution procedure. Such conditions are simply fulfilled by assigning the same code numbers to corresponding degrees of freedom related to the nodes on opposite sides of the unit cell. However, this requires that the mesh as well as the mesostructure have the appropriate periodicity. The examples presented next demonstrate the approach on such structures. Also, as mentioned earlier, the corners of the unit cell are all associated with the same point due to the double periodicity and are thus fully prescribed.

5. Examples

As an illustration and verification of the proposed model, we analyzed plane strain compression and plane strain simple shear deformations on a unit cell consisting of 40 randomly oriented grains. The overall effective stress-strain curve and texture evolution are compared with upper and lower
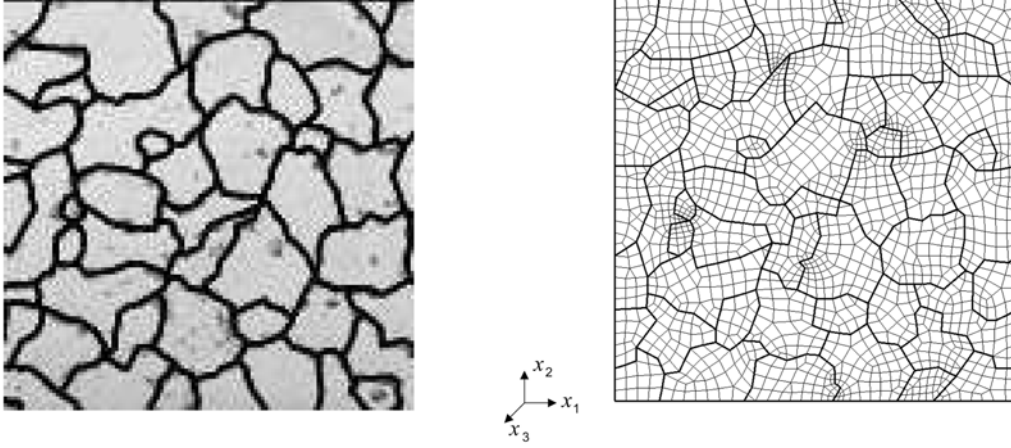
Fig. 5 a) The micrograph of an aluminum alloy

Fig. 5 b) The FE representation of the unit cell

Table 1 Elastic (Lamé parameters) and viscoplastic properties of Al-1100

μ_e [GPa]	λ_e [GPa]
25.30	54.41

m	g_0 [MPa]	$\dot{\gamma}_0$ [s^{-1}]	G_0 [MPa]	g_{s_0} [MPa]	$\dot{\gamma}_s$ [s^{-1}]	ω
0.005	27.17	1.0	58.41	61.80	5.0×10^{10}	5.0988×10^{-6}

bound analyses. The geometry of the selected RVE was motivated by a micrograph of an aluminum alloy (Misiolek 2002). This image, with highlighted grain boundaries, is shown in Fig. 5(a). Fig. 5(b) displays the finite element discretization of the selected unit cell. Note, that grains on boundaries of the unit cell were modified to allow for periodic boundary conditions. A periodic mixed mesh, primarily consisting of quadrilateral elements, was generated using the *T3D* mesh generator developed by Rypl and Bittnar (2002). A total of 1787 nodes, 104 triangles and 1656 quadrilaterals were used in the discretization of the 0.1×0.1 mm domain. We use $Q_1/P_0/V_0$ and $P_1/P_0/V_0$ elements in our simulations.

    The material behavior is as described in Eqs. (13-16) and (33-37). The properties are selected for Al-1100 at a temperature of 300 K and are listed in Table 1 (Mathur and Dawson 1989). The elastic anisotropy of the aluminum, which is small, is neglected in this analysis. Aluminum is face-centered-cubic, and the usual primary twelve {111} <$\bar{1}$10> slip systems are considered. The <111> pole figures depicting the initial random texture of the unit cell are shown in Fig. 6.

    The deformations considered, as mentioned above, are plane strain compression and simple shear. The time over which the total deformation occurs is denoted t_{tot}. The macroscopic deformation gradients associated with these deformations, assuming incompressible behavior, are for plane strain compression
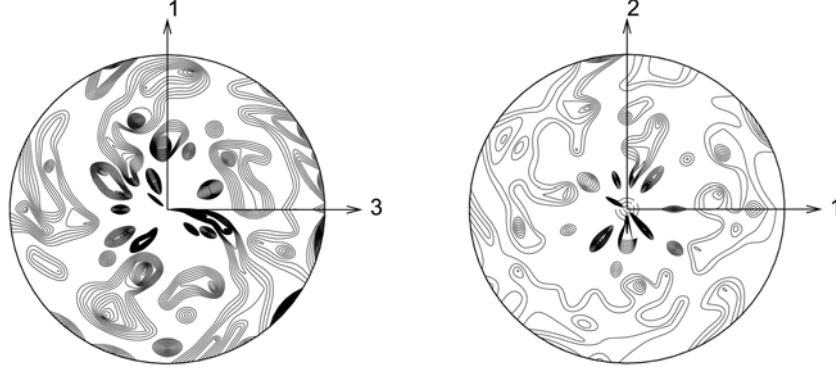
Fig. 6 The <111> pole figures of initial 40 grain orientations

$$\boldsymbol{F}_{n+1} = \begin{bmatrix} \dfrac{t_{tot}}{t_{tot} + t_{n+1}\breve{\varepsilon}} & 0 & 0 \\ 0 & 1 + \dfrac{t_{n+1}\breve{\varepsilon}}{t_{tot}} & 0 \\ 0 & 0 & 1 \end{bmatrix} \tag{46}$$

and for simple shear

$$\boldsymbol{F}_{n+1} = \begin{bmatrix} 1 & \dfrac{t_{n+1}\breve{\varepsilon}}{t_{tot}} & 0 \\ 0 & 1 & 0 \\ 0 & 0 & 1 \end{bmatrix} \tag{47}$$

where $\breve{\varepsilon} = \dfrac{\breve{u}}{l}$ and l is the length of a side of the unit cell. In the comparative analyses where the Taylor model (upper bound) was used, these deformation gradients were applied to each grain. Those simulations were carried out using the integration algorithm described in our previous work (Matou and Maniatty 2004) and the same results were obtained using the integration algorithm presented in Maniatty *et at.* (1992).

In the lower bound comparative simulations, the same Cauchy stress is applied to each grain.

The applied Cauchy stress is for plane strain compression

$$\boldsymbol{\sigma}_{n+1} = \begin{bmatrix} -\dot{\sigma}\, t_{n+1} & 0 & 0 \\ 0 & \dot{\sigma}\, t_{n+1} & 0 \\ 0 & 0 & 0 \end{bmatrix}$$

and for simple shear

$$\boldsymbol{\sigma}_{n+1} = \begin{bmatrix} 0 & \dot{\sigma}\, t_{n+1} & 0 \\ \dot{\sigma}\, t_{n+1} & 0 & 0 \\ 0 & 0 & 0 \end{bmatrix}$$

where $\dot{\sigma}$ is a constant stress rate taken to be 1 MPa/s in the examples that follow. The Cauchy stress at each time is not sufficient to give a unique solution for updating the state of the grain, i.e., computing ^eF, ^pF, and g. To see this, first express the velocity gradient using the multiplicative decomposition of the deformation gradient and performing a right polar decomposition on $^eF = {}^lR\,{}^eU$ resulting in

$$L = \dot{F}\,F^{-1} = {}^l\dot{R}\,{}^lR^T + {}^lR\,{}^e\dot{U}\,{}^eU^{-1}\,{}^lR^T + {}^lR\,{}^eU\,{}^p\dot{F}\,{}^pF^{-1}\,{}^eU^{-1}\,{}^lR^T \tag{48}$$

Now splitting the above into symmetric and skew parts yields

$$D = {}^lR({}^e\dot{U}\,{}^e\dot{U}^{-1})^{\mathrm{sym}}{}^lR^T + {}^lR\left[{}^eU\sum_{\alpha=1}^{\mathcal{N}_s}\dot{\gamma}(\tau^\alpha,g)\mathcal{P}^{\alpha e}U^{-1}\right]^{\mathrm{sym}}{}^lR^T$$

$$W = {}^l\dot{R}\,{}^lR^T + {}^lR({}^e\dot{U}\,{}^eU^{-1})^{\mathrm{skw}}{}^lR^T + {}^lR\left[{}^eU\sum_{\alpha=1}^{\mathcal{N}_s}\dot{\gamma}(\tau^\alpha,g)\mathcal{P}^{\alpha e}U^{-1}\right]^{\mathrm{skw}}{}^lR^T \tag{49}$$

where D and W are the rate of deformation and spin tensors, respectively. Now if the Cauchy stress is given and the current orientation is known, then the elasticity relation given in Eq. (33) can be inverted to determine $^eU = ({}^e\hat{C})^{-1/2}$, which in turn can be used to determine τ^α on each slip system using Eq. (34). Furthermore, if the resistance to plastic slip, g, is assumed known for the moment, then the rate of shearing can be computed on each slip system using Eq. (35). In addition, Eq. (36) could be used to update the resistance to plastic flow g. However, there still needs to be an update of the lattice orientation ^lR, which is typically done by solving Eq. (49b) for $^l\dot{R}$ and integrating forward in time using an update such as that presented in Simo and Vu-Quoc (1986). This update requires knowledge of the spin tensor, W. Thus, the spin tensor, in addition to the Cauchy stress tensor, needs to be prescribed. For the case of plane strain compression, the spin tensor is simply taken to be $W = 0$ to match the case with the prescribed deformation. For the case of simple shear, the spin tensor is taken to be

$$W = \begin{bmatrix} 0 & D_{12} & 0 \\ -D_{12} & 0 & 0 \\ 0 & 0 & 0 \end{bmatrix}$$

where D_{12} denotes the component of the rate of deformation tensor. This choice is made so that the resulting form of the velocity gradient matches that of the case with the prescribed deformation.

The resulting local and macroscopic behavior are characterized by the effective plastic strain and von Mises effective stress. The local effective plastic strain $^p\varepsilon_{eff}$ and effective stress σ_{eff} are computed as

$$^p\varepsilon_{eff} = \int_0^t \sqrt{\frac{2}{3}{}^p\hat{D}\cdot{}^p\hat{D}}\,dt'$$

and

$$\sigma_{eff} = \sqrt{\frac{3}{2}\sigma\cdot\sigma}$$

where

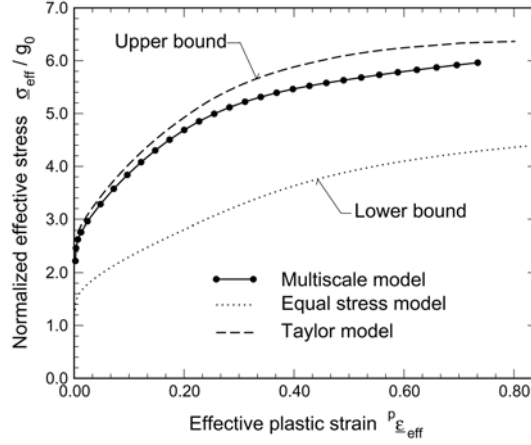$$^p\hat{D} \equiv \mathrm{sym}({}^p\hat{L})$$

Fig. 7 The overall effective stress-strain behavior for plane strain compression

The macroscopic response of the unit cell is described by the average rate of deformation and stress tensors, denoted by underline (−), which are computed as a volume averages of the local fields

$$
{}^{p}\underline{\hat{\boldsymbol{D}}} = \frac{1}{v}\int_{v}{}^{p}\hat{\boldsymbol{D}}\,\mathrm{d}\upsilon \qquad \underline{\boldsymbol{\sigma}} = \frac{1}{v}\int_{v}\boldsymbol{\sigma}\,\mathrm{d}\upsilon
$$

where υ is the volume of the deformed unit cell. The macroscopic effective plastic strain and stress are then computed analogously to the local fields as

$$
{}^{p}\underline{\varepsilon_{eff}} = \int_{0}^{t}\sqrt{\frac{2}{3}{}^{p}\underline{\hat{\boldsymbol{D}}}\cdot{}^{p}\underline{\hat{\boldsymbol{D}}}}\,\mathrm{d}t'
$$

and

$$
\underline{\sigma_{eff}} = \sqrt{\frac{2}{3}\underline{\boldsymbol{\sigma}}\cdot\underline{\boldsymbol{\sigma}}}
$$

First, consider the plane strain compression loading case. The unit cell is subjected to macroscopic plane strain compression, Eq. (46), over a time of $t_{tot} = 50$ s with $\overset{\smile}{\dot{u}} = -0.001$ mm/s constant and $\overset{\smile}{\varepsilon} = -0.5$, $\overset{\smile}{u} = -0.05$ mm. Fig. 7 shows the macroscopic effective stress strain curve from the multiscale analysis along with those predicted by the Taylor (upper bound) and equilibrium (lower bound) models for the same 40 grains. As expected the multiscale solution with periodic fluctuations lies between bounds. Fig. 8 shows the periodic deformation and mesoscopic effective plastic strain fields. As can be seen from Fig. 8, the effective plastic strain is also periodic and creates a shear band deformation pattern. The dotted line in Fig. 8 represents the homogeneous deformation as in the Taylor analysis. The predicted textures for both the Taylor and multiscale models at the final compression are displayed in Fig. 9. The models are in reasonable agreement, and the predicted texture corresponds qualitatively to that typically observed experimentally for plane strain compression of Al alloys. It should be also noted that the Taylor model, as the upper bound solution, is known to over-predict the final texture (Harren and Asaro 1989). Moreover, the contour plots of the normalized density function are plotted using more poles from the finite element model, where poles are contributed from each finite element integration point, and the poles
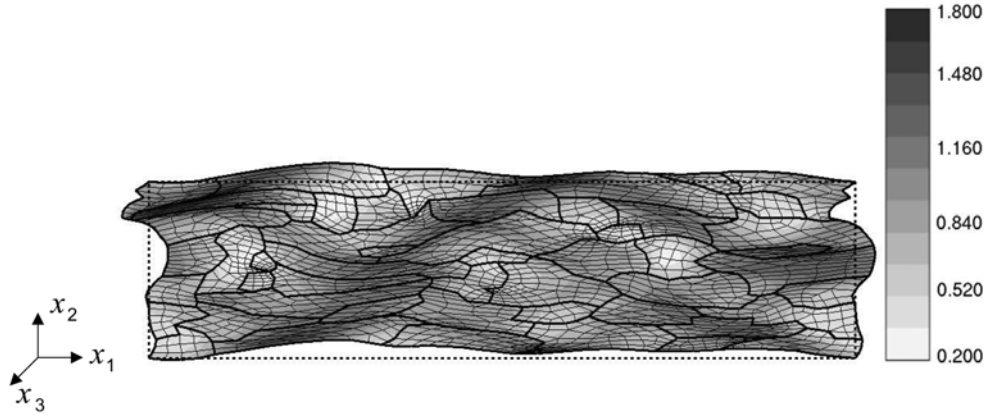
Fig. 8 The effective plastic strain $^{p}\varepsilon_{eff}$ after 50% plane strain compression of the unit cell, FE multiscale model prediction
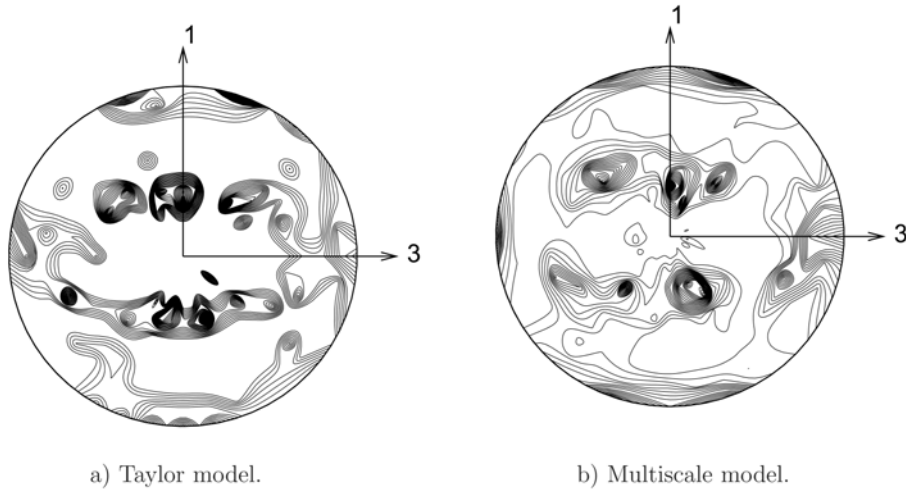

a) Taylor model.   b) Multiscale model.

Fig. 9 The <111> pole figure after 50% plane strain compression of the unit cell, comparison between the Taylor and FE multiscale models

spread out as the deformation proceeds since the grains deform non-homogeneously resulting in different parts of a single grain having different orientations, although each grain had a single orientation at the start. On the other hand, for the Taylor model, each grain has only a single orientation throughout the deformation due to the assumed homogeneous deformation within each grain.

In the second example, the RVE is loaded by a macroscopic deformation gradient corresponding to simple shear, Eq. (47). The macro-continuum is sheared by $\breve{\varepsilon} = 0.5$, $\breve{u} = 0.05$ mm over a time of $t_{tot} = 50$ s with $\dot{\breve{u}} = 0.001$ mm/s constant. As in the previous example, the macroscopic stress-strain response lies between bounds as shown in Fig. 10. Fig. 11 shows the mesoscale periodic effective strain field together with periodic deformation. The deformation is decomposed, as in the compression case, into homogeneous deformation (dotted line) and superimposed periodic
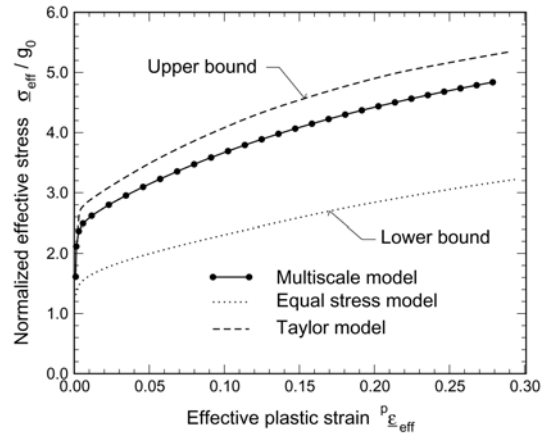
Fig. 10 The overall effective stress-strain behavior for plane strain simple shear
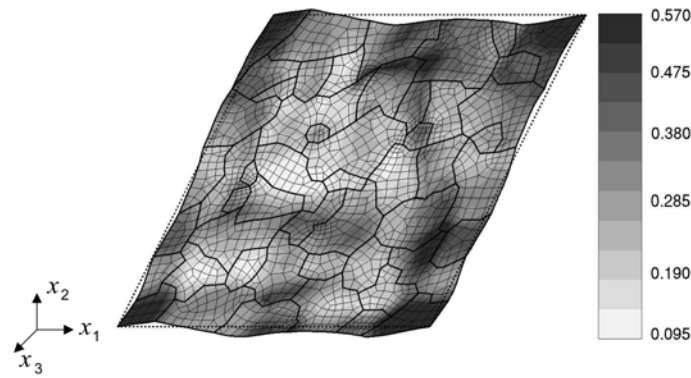

Fig. 11 The effective plastic strain $^{p}\varepsilon_{eff}$ after 50% plane strain simple shear of the unit cell, FE multiscale model prediction
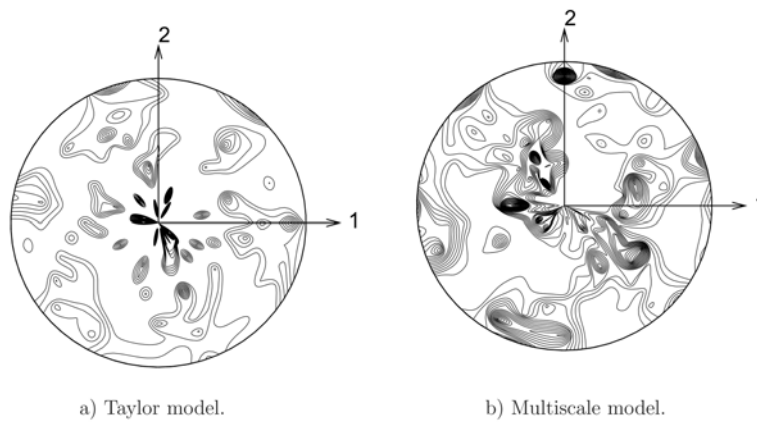

a) Taylor model.   b) Multiscale model.

Fig. 12 The <111> pole figure after 50% plane strain simple shear of the unit cell, comparison between the Taylor and FE multiscale models

fluctuation displacement field. The highest concentration of the effective plastic strain (Fig. 11) is accumulated within the corner crystal where the randomly assigned crystallographic orientation is favorable for plastic flow. Fig. 12 shows a comparison of <111> pole figures between the Taylor and the multiscale finite element models. The texture is not strongly developed in this case due to the continual rotation of the principle directions during the deformation. The main observation worth noting again is the spreading of the orientations in the multiscale analysis due to the nonhomogeneous deformations in the grains.

6. Conclusions

Computational procedures for the analysis of a homogenized macro-continuum with a locally attached periodic mesostructure of elastic-viscoplastic crystals were presented. The relationship between the behavior at the meso- and macroscales was discussed, and an incrementally linearized form of the macroscopic constitutive relations was derived.

The proposed multiscale formulation is shown to be effective in modeling elasto-viscoplastic behavior and texture evolution in a polycrystalline materials subject to finite strains. The mesoscale is characterized by a representative volume element and is capable of predicting local non-homogeneous stress and deformation fields. A realistic grain structure, motivated by experimental observations, is modeled with a displacement-based updated Lagrangian finite element formulation using the Hu-Washizu variational principle to create a stable method in the context of nearly incompressible behavior. The elastic behavior is defined by a hyperelastic potential, and the viscoplastic response is modeled by a simple power law complemented by a work hardening equation. A fully implicit two-level backward Euler integration scheme and the consistent linearization are used to obtain an efficient algorithm, where large time steps can be taken. The proposed multiscale analysis is capable of predicting non-homogeneous meso-fields, which, for example, may impact subsequent recrystal-lization.

Finally, examples are considered involving simple deformations of an aluminum alloy to predict inhomogeneous fields on the grain scale, and the macroscopic effective stress-strain curve and texture evolution are compared to those obtained using both upper and lower bound models.

Future work involves extending the method to 3D with a parallel implementation and using the model for more detailed studies. Further on-going studies are necessary to determine the minimum number of grains needed for a representative statistical sampling. The approach can be used to study the effect of local texture on local deformation. In addition, other crystal plasticity models can be implemented, and the approach can be used for supplying information for and validation of macroscale constitutive models.

References

Taylor, G.I. and Elam, C.F. (1925), "The plastic extension and fracture of aluminum crystals", *Proceedings of the Royal Society of London*, London, May.

Taylor, G.I. (1938), "Plastic strain in metals", *J. Inst. Metals,* **62**, 307-324.

Bishop, J.F.W. and Hill, R. (1951a), "A theory of the plastic distortion of a polycrystalline aggregate under combined stresses", *Philos. Mag.*, **42**, 414-427.

Bishop, J.F.W. and Hill, R. (1951b), "A theoretical derivation of the plastic properties of a polycrystalline face-centered metal", *Philos. Mag.*, **42**, 1298-1307.

Peirce, D., Asaro, R.J. and Needleman, A. (1983), "Material rate sensitivity and localized deformation in crystalline solids", *Acta Metall.*, **31**, 1951-1976.

Mathur, K.K. and Dawson, P.R., (1989), "On modeling the development of crystallographic texture in bulk forming processes", *Int. J. Plasticity*, **5**, 67-94.

Acharya, A. and Beaudoin, A.J. (2000), "Grain-size effect in viscoplastic polycrystals at moderate strains", *J. Mech. Phys. Solids*, **48**, 2213-2230.

Busso, E.P., Meissonnier, F.T. and O'Dowd, N.P. (1999), "Gradient-dependent deformation of two-phase single crystals", *J. Mech. Phys. Solids*, **48**, 2333-2361.

Asaro, R.J. and Needleman, A. (1985), "Texture development and strain hardening in rate dependent polycrystals", *Acta Metall.*, **33**, 923-953.

Maniatty, A.M., Dawson, P.R. and Lee, Y.S. (1992), "A time integration algorithm for elastoplastic cubic crystals applied to modelling polycrystalline deformation", *Int. J. Numer. Meth. Eng.*, **35**, 1565-1588.

Chastel, Y.B. and Dawson, P.R. (1993), "An equilibrium-based model for anisotropic deformations of polycrystalline materials", *Proceedings of the 10th International Conference on Textures of Materials*, Clausthal, September.

Molinari, A., Canova, G.R. and Azhi, A. (1987), "A self-consistent approach of the large deformation polycrystal viscoplasticity", *Acta Metall.*, **35**, 2983-2994.

Bay, B., Hansen, N., Hughes, D.A. and Kuhlmann-Wilsdorf, D. (1992), "Evolution of f.c.c. deformation structures in polyslip", *Acta Metall.*, **40**, 205-219.

Harren, S.V. and Asaro, R.J. (1989), "Nonuniform deformations in polycrystals and aspects of the validity of the Taylor model", *J. Mech. Phys. Solids*, **37**, 191-232.

Becker, R. (1991), "Analysis of texture evolution in channel die compression - I. Effects of grain interaction", *Acta Metal. Mater.*, **39**, 1211-1230.

Bronkhorst, C.A., Kalidindi, S.R. and Anand, L. (1992), "Polycrystalline plasticity and the evolution of crystallographic texture in fcc metals", *Philos. T. R. Soc. A.*, **341**, 443-477.

Marin, E.B. and Dawson, P.R. (1998), "On modelling the elasto-viscoplastic response of metals using polycrystal plasticity", *Comput. Meth. Appl. M.*, **165**, 1-21.

Sarma, G.B., Radhakrishnan, B. and Dawson, P.R. (2002), "Mesoscale Modeling of Microstructure and Texture Evolution During Deformation Processing of Metals", *Adv. Eng. Mater.*, **4**(7), 509-514.

Beaudoin, A.J., Acharya, A., Chen, S.R., Korzekwa, D.A. and Stout, M.G. (2000), "Consideration of grain-size effect and kinetics in the plastic deformation of metal polycrystals", *Acta Mater.*, **48**, 3409-3423.

Clayton, J.D. and McDowell, D.L. (2003), "A multiscale multiplicative decomposition for elastoplasticity of polycrystals", *Int. J. Plasticity*, **19**(9), 1401-1444.

Hashin, Z. and Shtrikman, S. (1962), "On some variational principles in anisotropic and nonhomogeneous elasticity", *J. Mech. Phys. Solids*, **10**, 335-342.

Hill, R. (1963), Elastic properties of reinforced solids: Some theoretical principles", *J. Mech. Phys. Solids*, **11**, 357-372.

Willis, J.R. (1989), "The structure of overall constitutive relations for a class of nonlinear composites", *IMA J. Appl. Math.*, **43**, 231-242.

Teply, J.L. and Dvorak, G.J. (1988), "Bounds on overall instantaneous properties of elastic-plastic composites", *J. Mech. Phys. Solids*, **36**, 29-58.

Hill, R. (1984), "On macroscopic effects of heterogeneity in elastoplastic media at finite strain", *Math. Proc. Cambridge Pholos. Soc.*, **95**, 481-494.

Hill, R. (1985), "On the micro-to-macro transition in constitutive analyses of elastoplastic response at finite strain", *Math. Proc. Cambridge Philos. Soc.*, **98**, 579-590.

Michel, J.C., Moulinec, P. and Suquet, P. (1999), "Effective properties of composite materials with periodic microstructure: a computational approach", *Comput. Meth. Appl. M.*, **172**, 109-143.

Miehe, C., Schröder, J. and Schotte, J. (1998), "Computational homogenization analysis in finite plasticity Simulation of texture development in polycrystalline materials", *Comput. Meth. Appl. M.*, **171**, 387-418.

Miehe, C., Schröder, J. and Becker, M. (2002), "Computational homogenization analysis in fi-nite elasticity:

material and structural instabilities on the micro- and macro-scales of periodic composites and their interaction", *Comput. Meth. Appl. M.*, **191**, 4971-5005.

Kouznetsova, V., Geers, M.GD. and Brekelmans, W.A.M. (2002), "Multi-scale constitutive modelling of heterogeneous materials with a gradient-enhanced computational homogenization scheme", *Int. J. Numer. Meth. Eng.*, **54**, 1235-1260.

Kristensson, O., Sørensen, N.J. and Andersen, B.S. (2003), "Concurrent finite element analysis of periodic boundary value problems", *Comput. Meth. Appl. M.*, **192**, 1877-1891.

Sundararaghavana, V. and Zabaras, N. (2006), "Design of microstructure-sensitive properties in elasto-viscoplastic polycrystals using multi-scale homogenization", *Int. J. Plasticity*, **22**(10), 1799-1824.

Ranganathan, S.I. and Ostoja-Starzewski, M. (2008), "Scaling function, anisotropy and the size of RVE in elastic random polycrystals", *J. Mech. Phys. Solids*, **56**, 2773-2791.

Lee, E.H. (1969), "Elastic-plastic deformation at finite strains", *J. Appl. Mech. ASME*, **36**, 1-6.

Hill, R. (1966), "Generalized constitutive relation for incremental deformation of metals crystals by multisplit", *J. Mech. Phys. Solids*, **14**, 95-102.

Lee, E.H. (1981), "Some comments on elastic-plastic analysis", *Int. J. Solids Struct.*, **17**, 859-872.

Matouš, K. and Maniatty, A.M. (2004), "Finite Element Formulation for Modeling Large Deformations in Elasto-viscoplastic Polycrystals", *Int. J. Numer. Meth. Eng.*, **60**, 2313-2333.

Simo, J.C., Taylor, R.L. and Pister, K.S. (1985), "Variational and projection methods for the volume constraint in finite deformation elasto-plasticity", *Comput. Meth. Appl. M.*, **51**, 177-208.

Hughes, T.J.R. (1980), "Generalization of selective integration procedures to anisotropic and nonlinear materials", *Int. J. Numer. Meth. Eng.*, **15**, 1413-1418.

Voce, E. (1948), "A practical strain-hardening function", *Acta Metall.*, **51**, 219-226.

Kocks, U.F. (1976), "Laws for work-hardening and low-temperature creep", *J. Eng. Mater-T ASME*, **98**, 76-85.

Moran, B., Ortiz, M. and Shih, C.F. (1990), "Formulation of implicit finite element methods for multiplicative finite deformation plasticity", *Int. J. Numer. Meth. Eng.*, **29**, 483-514.

Davis, T.A. and Duff, I.S. (1997), "An unsymmetric-pattern multifrontal method for sparse LU factorization", *SIAM J. Matrix Anal. A.*, **18**(1), 140-158.

Davis, T.A. and Duff, I.S. (1999), "A combined unifrontal/multifrontal method for unsymmetric sparse matrices", *ACM T. Math. Software*, **25**(1), 1-19.

Misiolek, W.Z. (2002), Private communication.

Rypl, D. and Bittnar, Z. (2002), "Hybrid Method for Generation of Quadrilateral Meshes", *Eng. Mech.*, **9**(1/2), 49-64.

Simo, J.C. and Vu-Quoc, L. (1986), "A three-dimensional finite-strain rod model. Part II: Computational aspects", *Comput. Meth. Appl. M.*, **58**, 76-116.